Chemical Engineering Science 271 (2023) 118550

Contents lists available at ScienceDirect

Chemical Engineering Science

journal homepage: www.elsevier.com/locate/ces

Ammonia decomposition in a dielectric barrier discharge plasma: Insights from experiments and kinetic modeling

J.A. Andersen [a], K. van 't Veer [b], J.M. Christensen [a], M. Østberg [c], A. Bogaerts [b], A.D. Jensen [a,*]

[a] Department of Chemical and Biochemical Engineering, Technical University of Denmark, 2800 Kgs. Lyngby, Denmark
[b] Research Group PLASMANT, Department of Chemistry, University of Antwerp, 2610 Wilrijk, Belgium
[c] Topsoe A/S, Haldor Topsøes Allé 1, 2800 Kgs. Lyngby, Denmark

HIGHLIGHTS

- The plasma achieved an NH_3 conversion of 82 % at a specific energy input of 18 kJ/Nl.
- NH_3 decomposition was found to be initiated by electron dissociation collisions.
- Higher energy transfer through micro-discharges promoted the NH_3 decomposition.
- Introduction of packing material resulted in a lower conversion of 37%.
- Re-formation of NH_3 occurred through an Eley-Rideal reaction with NH_2 and H(s).

ARTICLE INFO

Article history:
Received 16 November 2022
Received in revised form 13 January 2023
Accepted 5 February 2023
Available online 9 February 2023

Keywords:
Ammonia Decomposition
DBD Plasma
Clean Hydrogen
Chemical Kinetics Model
Micro-Discharges

ABSTRACT

Utilizing ammonia as a storage medium for hydrogen is currently receiving increased attention. A possible method to retrieve the hydrogen is by plasma-catalytic decomposition. In this work, we combined an experimental study, using a dielectric barrier discharge plasma reactor, with a plasma kinetic model, to get insights into the decomposition mechanism. The experimental results revealed a similar effect on the ammonia conversion when changing the flow rate and power, where increasing the specific energy input (higher power or lower flow rate) gave an increased conversion. A conversion as high as 82 % was achieved at a specific energy input of 18 kJ/Nl. Furthermore, when changing the discharge volume from 31 to 10 cm^3, a change in the plasma distribution factor from 0.2 to 0.1 was needed in the model to best describe the conversions of the experiments. This means that a smaller plasma volume caused a higher transfer of energy through micro-discharges (non-uniform plasma), which was found to promote the decomposition of ammonia. These results indicate that it is the collisions between NH_3 and the high-energy electrons that initiate the decomposition. Moreover, the rate of ammonia destruction was found by the model to be in the order of 10^{22} molecules/(cm^3 s) during the micro-discharges, which is 5 to 6 orders of magnitude higher than in the afterglows. A considerable re-formation of ammonia was found to take place in the afterglows, limiting the overall conversion. In addition, the model revealed that implementation of packing material in the plasma introduced high concentrations of surface-bound hydrogen atoms, which introduced an additional ammonia re-formation pathway through an Eley-Rideal reaction with gas phase NH_2. Furthermore, a more uniform plasma is predicted in the presence of $MgAl_2O_4$, which leads to a lower average electron energy during micro-discharges and a lower conversion (37 %) at a comparable residence time for the plasma alone (51 %).

1. Introduction

A global energy transition from fossil hydrocarbon-based energy sources to renewable energy sources such as wind and solar is currently underway. However, these renewable sources are highly weather-dependent, and efficient energy storage methods and energy carriers are therefore necessary (Hasan et al., 2021). Hydrogen (H_2) is considered a possible energy carrier as it is a clean and carbon-free energy source. However, delivery and storage issues for H_2 obstruct its implementation (Edwards et al., 2007). Other indirect storage media are therefore of interest for distribution. Ammonia (NH_3) is currently investigated as a storage medium for H_2 due to its ability to condense at 25 °C and ca.

* Corresponding author.
E-mail address: Aj@kt.dtu.dk (A.D. Jensen).

https://doi.org/10.1016/j.ces.2023.118550
0009-2509/

10 atm, which makes storage and distribution easier (Lamb et al., 2019; Salmon and Bañares-Alcántara, 2021; Schüth et al., 2012; Wan et al., 2021). Recently, Iriawan et al. (2021) reviewed existing and novel methods for producing ammonia by either reduction or oxidation. However, effective conversion processes must be developed for NH_3 to be utilized as a H_2 carrier.

Thermal NH_3 decomposition (see Reaction 1) has been an ongoing research area where reaction temperatures above 500 °C and a catalyst are used to achieve sufficient conversion. Different metals have been studied for the reaction, such as Fe, Ni, Mo, Co, Pt, Pd, and Rh, as well as different two-component combinations of these metals (Silva et al., 2015; Klerke et al., 2009; Lendzion-Bielun et al., 2013; Lucentini et al., 2021; Simonsen et al., 2012; Zheng et al., 2008).

$$2NH_3 \rightarrow 3H_2 + N_2\ ,\ \Delta_r H = 46.2\text{kJ/mol} \quad \text{(R1)}$$

An alternative to thermal activation could be electrical activation by plasma, which further promotes the green energy transition, as renewable energy sources can be used to power the plasma (Bogaerts and Neyts, 2018; Conrads and Schmidt, 2000). Various plasma types can be used, but dielectric barrier discharges (DBDs) in combination with different packing materials have received significant attention lately for the conversion/synthesis of various chemicals such as methane, carbon dioxide, and ammonia (Bogaerts, 2019; Bogaerts et al., 2020; Snoeckx and Bogaerts, 2017; Whitehead, 2016). Recently, an enhanced ability for NH_3 decomposition (Reaction 1) was reported (Akiyama et al., 2018; Andersen et al., 2022; El-Shafie et al., 2021, 2020; Hayakawa et al., 2020; Wang et al., 2019, 2017,2015; Yi et al., 2019).

Akiyama et al. (2018) proposed that the NH_3 decomposition only proceeds in the plasma atmosphere, as a common linear correlation between power and conversion was found when different wool-like, metallic (Ag, Al, Cu, Fe, and Ti) inner electrodes were utilized. Our recent work (Andersen et al., 2022) showed a linear correlation between the number of micro-discharges and the conversion, independent of packing material (except for a fully metallic Fe-based packing), indicating that the decomposition primarily proceeds in the gas phase through collisions with high-energy electrons. Wang et al. (2015) reported that the rate-limiting step in plasma-catalytic decomposition of NH_3 over metals (Fe, Co, Ni, and Cu) is the recombinative desorption of adsorbed N atoms. In another study, Wang et al. (2017) suggested that the plasma pre-activates the NH_3 by forming an electronically excited state (NH_3^*) which accelerates the adsorption and improves the conversion. Yi et al. (2019) similarly argued that pre-activation of NH_3 and formation of radicals (NH_2 and NH) by the plasma plays a crucial role for increasing the activity, as well as the catalyst capability to adsorb these species. Hayakawa et al. (2020) showed that by removing the produced H_2, an increased NH_3 conversion occurred. This indicates that the reverse reaction of Reaction 1 limits the NH_3 conversion in a plasma environment. This is not surprising since studies have shown that NH_3 can be synthesized from H_2 and N_2 in a plasma (Bai et al., 2003; Engelmann et al., 2021; Hong et al., 2018; van 't Veer et al., 2020a).

As discussed above, it is clear that different processes for NH_3 decomposition in a plasma are claimed to be vital, however, only little is known about the underlying reactions that drive the NH_3 decomposition. Hence, there is a clear need for a more detailed understanding. The cited studies investigating NH_3 decomposition are all experimental, and only in some of these papers, attempts were made to interpret the data based on simple chemical reactions assumed from the literature to occur in the DBD reactor.

In this work, we present a combined experimental study, utilizing a DBD reactor, and a plasma kinetic model, to improve the understanding of the reaction mechanism of NH_3 decomposition in such a DBD plasma. In the experimental part, the influence of plasma power, frequency, feed flow rate, residence time, and the presence of packing material in the discharge zone were examined for a diluted NH_3 feed stream. The plasma characteristics, recorded in the experiments, were used as input to the zero-dimensional (0D) plasma kinetic model, where special attention was paid on separating the effects of the micro-discharges and their afterglows in the assessment of the reaction mechanisms.

2. Experimental

Experiments were performed in a coaxial quartz DBD reactor setup described in detail elsewhere (Andersen et al., 2022). A stainless steel rod (ø: 10 mm) was utilized as the inner electrode, while a stainless steel mesh wrapped around the reactor worked as the outer electrode. This steel mesh had a varying length of 1–15 cm, to evaluate the effect of the size of the plasma volume (defining the residence time). The quartz tube reactor had an outer and inner diameter of 22 and 19 mm, respectively. The discharge gap between the inner electrode and the reactor wall was 4.5 mm. A TREK high voltage amplifier (model 20/20C-HS), controlled by a Tektronix function generator (AFG1022), was used to power the outer electrode. A Tektronix high voltage probe (P6015A), a Pearson Rogowski coil (4100), and an external capacitor (10 nF) with a Picotech low voltage probe (TA150) were used to measure the applied voltage, current, and generated charges, respectively. The voltage, current, charge, and calculated plasma power were continuously recorded by a Picotech digital oscilloscope (Picoscope 6402C).

Mass flow controllers (Bronkhorst) were used to pass a N_2 flow through the reactor for 10 min to remove any oxygen prior to each experiment. A feed mixture of 2.02 mol% NH_3 in N_2 at a flow rate of 50–125 Nml/min was then fed to the reactor. After 20 min of feeding the mixture, the plasma was ignited. The effluent was diluted in N_2 to a total flow rate of 1 Nl/min to comply with the flow requirement of the analyzer. The diluted flow was then analyzed using an online NH_3-analyser (ABB, AO2000-Limas 11 HW gas analyzer) to determine the concentration of the remaining NH_3. The decomposition was carried out at different plasma power values of 10–25 W, at a constant frequency of 3.0 kHz, and at different frequencies in the range of 1.0–3.5 kHz, at a constant plasma power of 15 W.

For experiments with packing material, $MgAl_2O_4$ pellets were crushed and sieved to a particle size of 0.85–1.4 mm and an outer electrode length of 5 cm, corresponding to a discharge volume of ca. 10 cm^3, was used. The physicochemical properties of $MgAl_2O_4$ were reported in our previous work (Andersen et al., 2022). The plasma zone was fully packed for the packed-bed experiments, corresponding to ca. 10 g of material. Glass wool was placed on each side of the bed to hold the material in place. All experiments were conducted at atmospheric pressure without external heating, with a plasma power stabilization period of 1 h after plasma ignition.

The conversion (X) of NH_3 was calculated according to Eq. (1) and the specific energy input (SEI) is defined as the plasma power over the total volumetric flow rate measured at nominal conditions (Eq. (2)). The NH_3 concentration in the reactor effluent was determined when the online analyzer showed a stable signal by taking an average over a 15-minute period. The average value was then used to calculate the conversion by Eq. (1).

$$X_{NH_3}(\%) = \frac{\text{Moles of } NH_3 \text{ in} - \text{Moles of } NH_3 \text{out}}{\text{Moles of } NH_3 \text{ in}} \cdot 100\% = \frac{NH_3 \text{converted}}{NH_3 \text{ in}} \cdot 100\% \quad (1)$$

$$\text{SEI (J/Nml)} = \frac{\text{Plasma power } \left[\frac{\text{J}}{\text{s}}\right] \cdot 60 \left[\frac{\text{s}}{\text{min}}\right]}{\text{Total flow rate } \left[\frac{\text{Nml}}{\text{min}}\right]} \quad (2)$$

3. Computational method

The 0D plasma kinetics solver ZDPlasKin (Pancheshnyi et al., 2008) was used in this study. The solver is coupled to BOLSIG+ (Hagelaar and Pitchford, 2005), which is a numerical solver for the steady state Boltzmann equation for electrons. BOLSIG + uses the collision cross sections, the ratio of the electric field (E) to the total number density of gas phase species (N) (i.e., reduced electric field (E/N)), and the gas temperature as inputs. The reduced electric field and the gas temperature were determined from experimental measurements, with N determined from the ideal gas law (pressure and temperature) and E from power density and electron conductivity (see equations Eq.S1-Eq.S6 in the Supporting Information, section S.2). The parameters used to determine the power density and electron conductivity are the charge transfer (Q_0), burning voltage (ΔU), capacitance of the cell (C_{cell}), effective capacitance (ζ_{diel}), and dielectric capacitance (C_{diel}), which are determined from the voltage and charge measurements (see Supporting Information, section S.2). The gas temperature was determined with a thermocouple placed on the outside of the reactor wall as described in Andersen et al. (2022), and was measured to be ca. 100 °C, independent of the length of the outer electrode. The gas mixture ratio of 98/2 N_2/NH_3 used in our experiments was also used as input. The plasma kinetic model was previously used to investigate plasma-based NH_3 synthesis (van 't Veer et al., 2020b, 2020a), but in this study, the model was used for plasma-based NH_3 decomposition, where the same plasma chemistry is expected to occur.

Collisions between electrons, so-called heavy particles (i.e., molecules, atoms, radicals, excited species and ions), and surfaces are considered to take place in the plasma. The plasma chemistry included in the model therefore considers the corresponding atoms, radicals, ions, and vibrationally and electronically excited states, which could appear during the decomposition, Reaction 1, along with empty surface sites and surface-adsorbed species, as listed in Table 1. Rate coefficients taken from the literature are used in the kinetic model to calculate the time-dependent density development of the gas and surface species. In the recent work by van 't Veer et al. (2020a) it was specifically noted that the surface kinetics is associated with uncertainty, that is, the exact properties of the surface. It was further discussed that assumptions were made for the Eley-Rideal (ER) sticking coefficients, due to the lack of reliable kinetic data, hence the surface described in the model was iron, simply for reference (van 't Veer et al., 2020a). In the present work, $MgAl_2O_4$ is used as the packing material due to its high synergy for plasma-catalytic NH_3 decomposition reported in our previous work (Andersen et al., 2022). Here, it was also reported that the surface reactions might not have a significant impact on the decomposition. The acquired results from the plasma kinetic model when including packing material are therefore primarily used to understand the effect of the surface reactions, and how the plasma characteristics, which are different in the presence of packing material, affect the decomposition in the gas phase. A full list of the gas phase and surface kinetics was reported by van 't Veer et al. (2020a, 2020b).

A surface site density of 10^{15} cm^{-2} is assumed in the model, to represent a generic surface (Cortright and Dumesic, 2001). Furthermore, an experimental reactor-specific volume-to-surface area ratio is used to convert the rate coefficients of the surface reactions from s^{-1} to $cm^3\ s^{-1}$ or $cm^6\ s^{-1}$. Here, the surface area is the sum of the outer surface of the particles, reactor wall, and inner electrode surface area. Note that only the outer surface area of the particles is used to determine this factor, since the plasma is not expected to propagate into the pores of the material (Zhang and Bogaerts, 2018). The outer surface area of the particles is calculated by assuming the shape of the particles to be an equal mixture of spheres and cylinders with radius and height determined from the specified particle size. This assumption was made based on visual inspection of the particles. A specific reactor volume-to-surface area ratio of 0.225 cm and 0.0143 cm was determined for the unpacked and packed setup, respectively.

A unique feature of the model is the inclusion of the spatial and temporal nature of micro-discharges developed by van 't Veer et al. (2020b). In the model, the power distribution factor (γ) is used to define the power density distribution between micro-discharges and a uniform plasma, with $\gamma = 1$ yielding a fully uniform plasma. Compared to the micro-discharges, the uniform plasma is a weaker plasma that is continuously present throughout the whole reactor. γ is determined based on the appearance of the experimental power profile (see Fig. 1), such that the power of the micro-discharges and of the uniform plasma in the model is in agreement with the experiments. However, as seen in Fig. 1, not all the micro-discharges have the same maximum power and the power of the uniform plasma is also not constant. Therefore, it is not possible to obtain an exact agreement between the ratio of power transferred to the micro-discharges and to the uniform plasma; hence several values of γ could be considered to characterize the plasma, as illustrated in Fig. 1.

The different discharge lengths tested and their corresponding residence times are shown in Table 2. Here, the number of micro-discharges per half cycle (N_{MD}) is also shown, along with the lifetime of a single micro-discharge (τ_{MD}). These values were experimentally determined by analyzing the current characteristics obtained from the digital oscilloscope.

A triangular power density pulse with the experimentally determined lifetime is used to model the micro-discharges. The power profiles used as input in the model, for different values of γ, are shown in Fig. 1 for the case of a discharge length of 5 cm over two half cycles. Here, it is observed that γ = 0.05 yields a better fit for the higher energy micro-discharges, as expected. Yet, this value overshoots the power for a significant part of the micro-discharges, where γ = 0.1 and 0.2 show a better fit. Additionally, γ = 0.1 and 0.2 show a better fit for the uniform plasma in the time period where micro-discharges occur (difficult to see on Fig. 1 due to the scale).

The plasma kinetic model assumes that the micro-discharges are uniformly distributed in time and in the plasma. A single molecule therefore cannot be affected by all the micro-discharges. Hence, a factor that determines how many micro-discharges a

Table 1
Overview of the species used in the model, with surface-adsorbed species indicated by (s).

Ground state molecules	Vibrationally excited states	Electronically excited states	Ions	Surface-adsorbed species
N_2, N H_2, H NH, NH_2, NH_3	$N_2(V = 1...24)$ $H_2(V = 1...14)$	$N_2(a'^1\Sigma_u^-)$, $N_2\left(A^3\Sigma_u^+\right)$, $N_2\left(B^3\Pi_g\right)$, $N_2\left(C^3\Pi_u\right)$ $H_2\left(a^3\Sigma_g^+\right)$, $H_2\left(b^3\Sigma_u^+\right)$, $H_2\left(B^1\Sigma_u^+\right)$, $H_2(c^3\Pi_u)$ $N\left(^2D^0\right)$, $N\left(^2P^0\right)$	N^+, N_2^+, N_3^+, $N_4^+H^+$, H_2^+, H_3^+, H^- N_2H^+, NH^+, NH_2^+, NH_3^+, NH_4^+	$N(s)$, $H(s)$ $NH(s)$, $NH_2(s)$

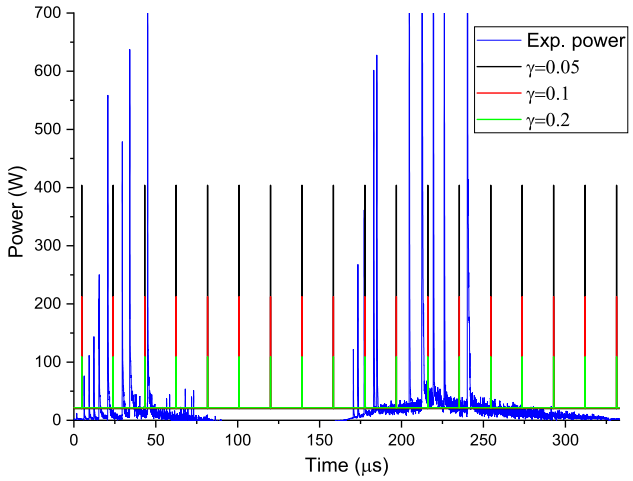

Fig. 1. Experimental plasma power as a function of time, and the model interpretation using different values of γ, for a full voltage cycle, with a frequency of 3 kHz at a discharge length of 5 cm.

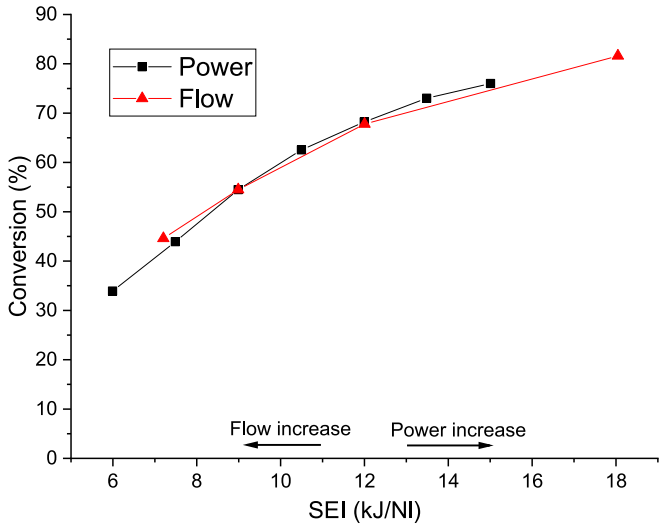

Fig. 2. NH_3 conversion as function of SEI obtained after 1 h, with either varying plasma power (at constant flow rate of 100 Nml/min) or varying flow rate (at constant power of 15 W), at a frequency of 3 kHz and a discharge volume of 10 cm^3.

molecule is exposed to is therefore introduced, as the time of a full discharge period divided by the residence time of the gas (van 't Veer et al., 2020b). Furthermore, the volume of a micro-discharge when no packing is present is modelled as a cylinder, as described by Equation 3, where h is the gap size (4.5 mm) and r is the radius of the micro-discharge, which has been reported to be in the order of 0.1 mm (Bogaerts et al., 2016).

$$V_{MD} = \pi \cdot h \cdot r^2 \quad (3)$$

When packing material is included, the volume of a micro-discharge is modelled as a spherical volume between solid particles (van 't Veer et al., 2020b). For this calculation, a packing factor of 0.68 is used to define the gas volume available in the reactor. This factor was determined experimentally by finding the displaced volume of water by the $MgAl_2O_4$ packing, after the pores of the material were first saturated with water.

4. Results and discussion

4.1. NH_3 conversion as function of flow rate, power, and frequency

Fig. 2 shows the results obtained from varying the plasma power and feed flow rate when conducting the decomposition in plasma-only. It is clear that when the SEI increases, hence more energy per molecule is applied, the conversion of NH_3 increases, which is similar to the results observed by Akiyama et al. (2018) and El-Shafie et al. (2021). The highest conversion achieved was 82 % at a SEI of 18 kJ/Nl. Both curves show a decreasing slope with increasing SEI, which corresponds to a decreasing energy efficiency. Interestingly, the two conversion curves, obtained by either changing the power or the feed flow rate, show similar results for the majority of the SEI values tested, even though the change in feed flow rate causes a change in residence time, which the power alteration does not. The effect of changing the residence time is discussed further in Section 4.2. A lower power yields a lower conversion. The lower power is the result of a lower applied voltage that will give a weaker electric field and therefore a lower acceleration of the electrons. The electron/molecule collisions will thereby transfer less energy and generally lead to fewer collisions giving rise to less decomposition.

The effect of altering the frequency is shown in Fig. 3. Here, a nearly linear increase in conversion with increasing frequency is observed, hence weaker, but more frequent energy pulses favor NH_3 decomposition. Increasing the frequency reduces the number of micro-discharges per half cycle (see Table S1), but on a time basis the number is higher. This indicates that collisions with the high-energy electrons initiate the decomposition, as the higher frequency leads to a larger number of micro-discharges for the full residence time. Therefore, a larger number of molecules can potentially interact with the micro-discharges and dissociate. This correlates with the observation in our recent work (Andersen et al., 2022), where the number of micro-discharges was found to be a determining factor for the conversion of NH_3.

4.2. NH_3 conversion as function of residence time

The effect of the gas residence time was investigated by altering the length of the outer electrode, hence the length of the discharge zone. In contrast to changing the residence time by changing the flow rate, this method does not alter the SEI for a fixed power input.

The experimentally determined NH_3 conversion as function of the gas residence time for a power input of 15 W is shown in Fig. 4 (black curve). A maximum conversion of 54 % is observed

Table 2
Reactor and micro-discharge specification used in the model.

	Discharge length [cm]	Gas residence time [s]	N_{MD}	τ_{MD}[ns]
No packing	1	1.25	8	200
No packing	2	2.50	9	200
No packing	5	6.25	9	200
No packing	10	12.5	9	200
No packing	15	18.8	9	200
Packed	5	2.00	30	200

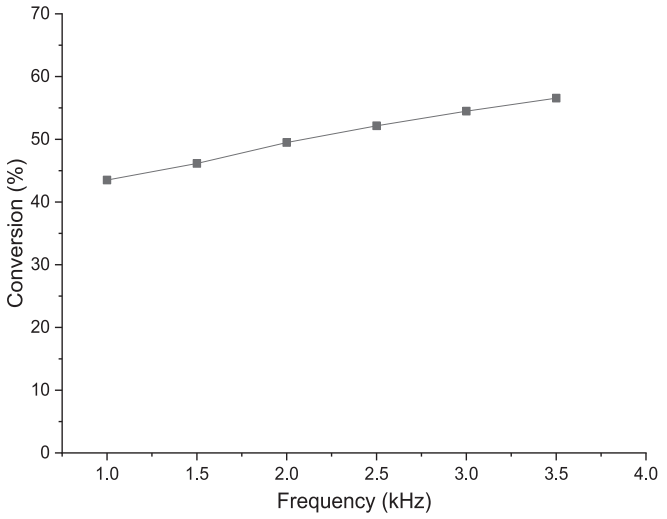

Fig. 3. NH_3 conversion as function of frequency obtained after 1 h, at a plasma power of 15 W and flow rate of 100 Nml/min (corresponding to an SEI of 9 kJ/Nl) and a discharge volume of 10 cm^3.

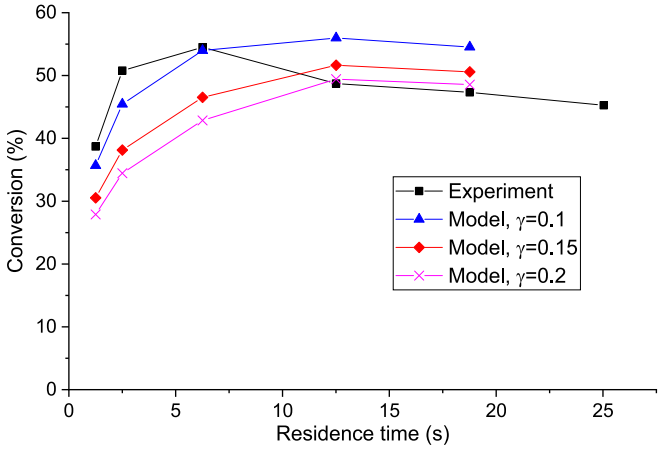

Fig. 4. NH_3 conversion as function of residence time obtained by changing the outer electrode length. Experimental data obtained after 1 h at a plasma power of 15 W and frequency of 3 kHz, flow rate of 100 Nml/min (corresponding to SEI of 9 kJ/Nl), and discharge gap of 4.5 mm. Results determined from the kinetic model were calculated for the case-specific parameters listed in Table 2 and Table S2 for various values of γ.

at a residence time of 6 s. For residence times between 12.5 and 25 s the conversion only changes slightly, indicating that a balance between the decomposition and re-formation of NH_3 could have been established at a conversion around 47 %. It must be mentioned, that ΔU decreases as the residence time (length of the outer electrode) is increased, see Table S2. A lower ΔU, results in a weaker electric field, and therefore a lower average energy of the electrons, which could be the reason for the decrease in conversion between the residence times of 6 and 12.5 s.

Additionally, Fig. 4 shows calculated NH_3 conversions using different values of the power density distribution factor. Using a value of γ equal to 0.2 predicts clearly lower conversion in the residence time range from 1 to 10 s than observed experimentally. However, at residence times of 12.5 and 18.8 s, the predicted conversions are very close to the experimental values. Lowering the value of the power density distribution factor to 0.15 and 0.1 increases the conversion for all investigated residence times, and with γ equal to 0.1, the model predicts the experimental conversions at residence times up to 6 s reasonably well. Nevertheless, for the shorter residence times (1 and 2.5 s), the modelled conversions remain lower than the experimental values, indicating that even less power is admitted to the uniform plasma. The model therefore predicts a change in the plasma distribution behavior (between micro-discharges and more uniform plasma) when the discharge volume is altered, and that having a more non-uniform plasma, i.e. lower γ, characterized by more intense micro-discharges (see Fig. 1 above), promotes the decomposition. This observation is consistent with the high-energy electrons initiating the decomposition, as a lower γ results in a higher density of electrons during the micro-discharges, as seen in Figure S1a in the Supporting Information obtained for a residence time of 6.25 s. Here, the electron density suddenly peaks in the course of a micro-discharge pulse, as expected. The reduced electric field and the temperature of the electrons show similar behavior as the electron density, with lower γ resulting in higher peak values, see Figures S1b and S1c, hence the mean electron energy during micro-discharges changes with γ. The change in conversion is therefore not only an effect of residence, but also an effect of altering the power distribution between micro-discharges and the uniform plasma, which comes from varying the plasma volume (electrode length).

4.3. Introduction of packing material

Packing the discharge zone with a material with a dielectric constant below 26 has previously been shown to improve the decomposition of NH_3 when treating a pure NH_3 feed (Andersen et al., 2022; Wang et al., 2015). In the present study, where a gas feed with 2 mol% NH_3 was examined, the introduction of the $MgAl_2O_4$ packing (dielectric constant of 8.3 (Shannon and Rossman, 1991)) was found to decrease the NH_3 conversion (X_{NH_3} = 37 %) compared to the empty reactor (X_{NH_3} = 51 %) at a comparable residence time (2.5 s in the empty reactor versus 2.0 s with packing) and identical power of 15 W as shown in Fig. 5. It must be noted that the reduction in residence time below 2.5 s could have an impact on the NH_3 conversion, as observed in Fig. 4. However, the empty reactor still shows a slightly higher conversion at a residence time of 1.25 s (X_{NH_3} = 39 %), hence another

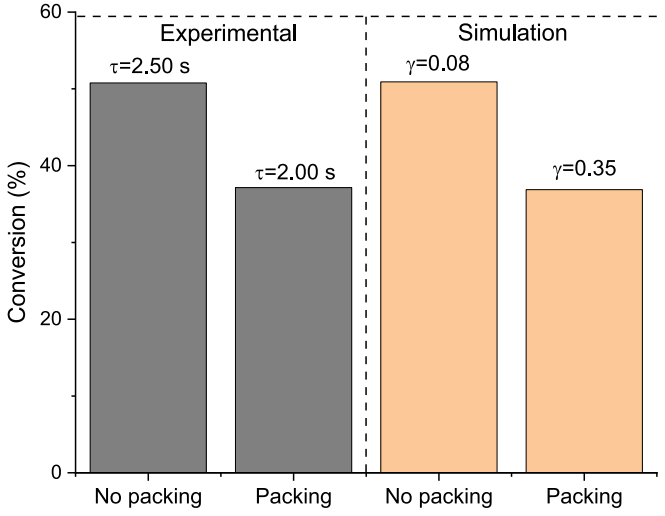

Fig. 5. NH_3 conversion when implementing $MgAl_2O_4$ packing in the plasma zone, found from experiments and simulations, compared with the NH_3 conversion obtained from an empty reactor at a similar residence time. Plasma power 15 W and frequency of 3 kHz, flow rate of 100 Nml/min, and discharge gap of 4.5 mm. In the model, the effect of the packing is simulated by using a higher γ of 0.35, corresponding to a more uniform plasma, in line with the model developed by van't Veer et al. (2020b).

parameter must also affect the conversion. It must further be noted that on Fig. 5, the outer electrode length for the empty reactor corresponding to the residence time of 2.5 s is 2 cm, but for the packed reactor, an electrode length of 5 cm was used to yield a (comparable) residence time of 2.0 s.

A larger number of micro-discharges per half cycle was present when packing material was introduced in the discharge zone, as indicated in Table 2. Here, the electron energy is significantly higher compared to the afterglows (see Figure S2). However, this was not found to have a positive effect, even though it was observed for the empty reactor that the high-energy electrons from the micro-discharges were mainly contributing to the decomposition. Interestingly, the average electron energy during the afterglows was predicted by the model to be slightly lower for the packed setup than for the unpacked. Additionally, the total number of electrons was predicted by the model to be higher for the packed setup over the full course of the gas residence time (see Figure S3), even though γ was found to increase to 0.35, meaning that a more uniform plasma was promoted by the $MgAl_2O_4$ packing (see Figure S4 for I-V measurements for the plasma-only and packed with $MgAl_2O_4$). Moreover, the increased N_{MD} was found to lower the duration of the afterglows, which in turn affects the reactions occurring in this period. This could mean that the enhanced electric field and the larger number of micro-discharges are not the only two factors dominating the conversion when introducing packing material. Plasma reactions with and without packing material will be discussed further below.

4.4. Plasma species densities and surface coverage

The transient behavior of the densities of selected gas phase species, as predicted from the model, is shown in Fig. 6, for the unpacked and packed reactor, with residence time of 2.5 s (γ = 0.08) and 2.0 s (γ = 0.35), respectively. Fig. 6a and 6c depict the neutral and vibrationally excited species during two micro-discharges and their afterglows, while Fig. 6b and 6d displays the radicals and charged species.

For the unpacked reactor, it is seen that the afterglow of a micro-discharge lasts approximately 120 ms, which is 6 orders of magnitude longer than the lifetime of the micro-discharges (ca. 200 ns). The time in plasma shown in Fig. 6a and 6b corresponds to the seventh and eighth micro-discharge encountered by a molecule. After this, only small variations in the concentrations are observed between micro-discharges for the species plotted in Fig. 6b, while for the neutral species, the NH_3 concentration slowly decreases, and as a result the N_2 and H_2 concentrations increase. The full transient density development for the unpacked and packed setup is shown in the Supporting Information (Figures S5 and S6).

The high density of N_2 observed in Fig. 6a is due to the feed composition used, and as a result, the density of vibrationally excited N_2 (N_2(v)) species is predicted to be in the order of $2x10^{18}$ to $7x10^{18}$ molecules/cm^3, since the main consumption of N_2 in micro-discharges (indicated by md) is by vibrational excitation (Reaction 2). In the afterglow (indicated by ag), N_2 is primarily

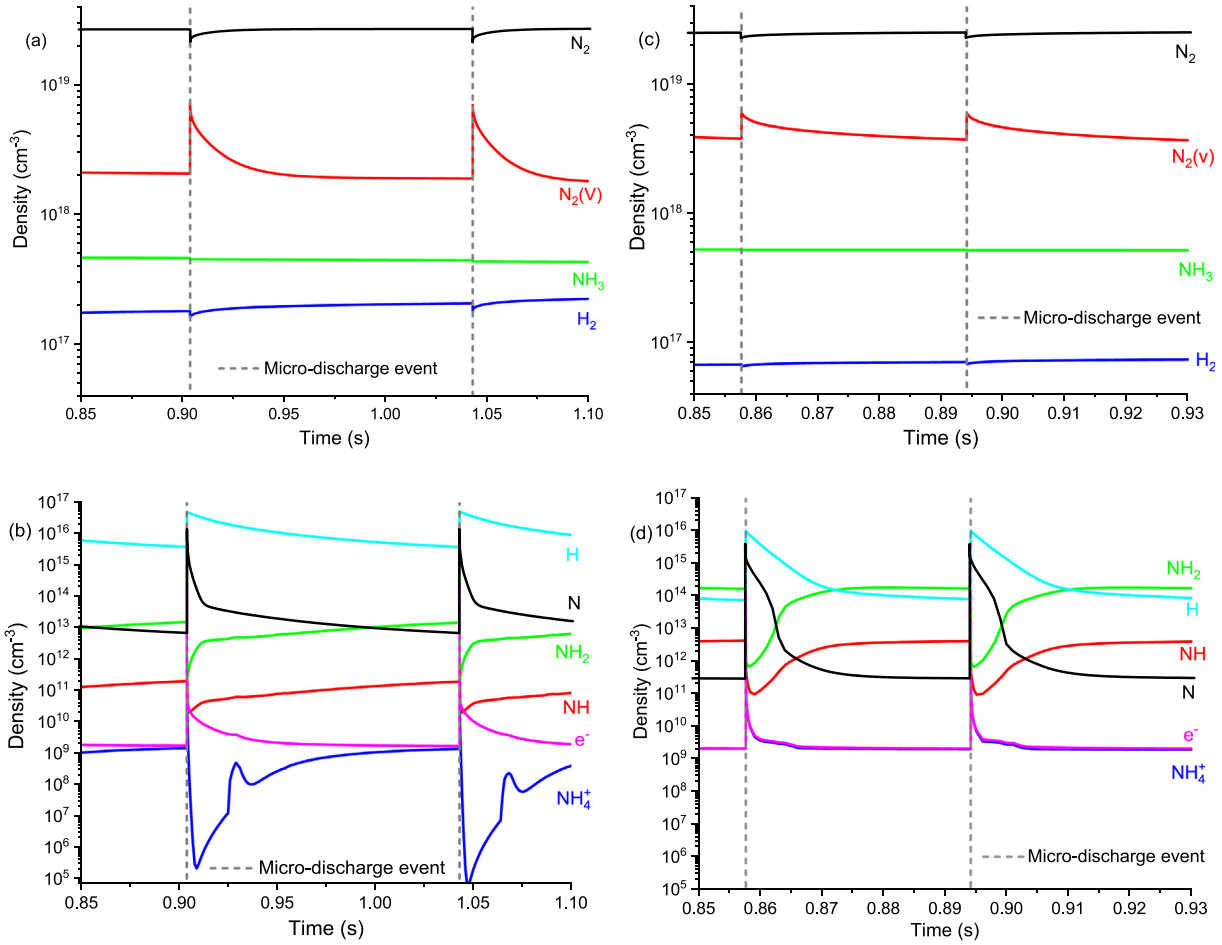

Fig. 6. Calculated number density as a function of time for unpacked plasma (outer electrode length of 2 cm and γ = 0.08) of (a) neutral and vibrationally excited species and (b) radicals and charged species in the gas phase, and similarly for packed plasma (outer electrode length of 5 cm and γ = 0.35) of (c) neutral and vibrationally excited species and (d) radicals and charged species.

predicted to collide with $N_2(v)$ of a higher vibrational state, resulting in the formation of two $N_2(v)$ of a lower vibrational state (Reaction 3). Simultaneously with Reaction 3, the $N_2(v)$ species decay to N_2 at a slow rate, explaining the long falloff and slow rise of $N_2(v)$ and N_2, respectively, in Fig. 6a. Furthermore, the density of NH_3 is decreasing slowly (barely visible on Fig. 6a), while H_2 has a net drop in the micro-discharges and a net rise in the afterglows.

$$(\text{md})\quad N_2 + e^- \rightarrow N_2(v) + e^- \tag{R2}$$

$$(\text{ag})\ N_2 + N_2(v) \rightarrow 2N_2(v) \tag{R3}$$

From Fig. 6b it is clear that H atoms have the highest density of the radicals, which increases during a micro-discharge to a value of ca. $5x10^{16}$ molecules/cm^3 and then slowly decreases in the afterglow to a value of ca. $4x10^{15}$ molecules/cm^3. The H atoms are predicted to have a density approximately 600 times higher than the N atoms during the afterglow and 5 times higher during a micro-discharge, even though the N_2 density is approximately-two orders of magnitude higher than that of H_2. This is attributed to the higher bond strength of N_2 (9.8 eV) compared to H_2 (4.5 eV) (Hong et al., 2018). The high difference in density between N and $N_2(v)$ is also a result of the large difference between the formation energy of the species (9.8 eV for N and 0.29 eV for $N_2(v = 1)$ and 0.57 eV for $N_2(v = 2)$). Interestingly, the formation of H atoms during a micro-discharge is mainly a result of collisions between electronically excited N_2 and H_2 (Reaction 4) and not from direct splitting of NH_3. However, obviously, H_2 is first produced from NH_3, as it is not introduced as feed gas. Furthermore, during the afterglow, the splitting of NH_3 (Reaction 5) and NH_2 (Reaction 6) contribute equally to the H formation as the previous collision reaction (Reaction 4).

$$(\text{md})/(\text{ag})\quad N_2\left(a'^1\Sigma_u^-\right) + H_2 \rightarrow 2\,H + N_2 \tag{R4}$$

$$(\text{ag})\ e^- + NH_3 \rightarrow e^- + NH_2 + H \tag{R5}$$

$$(\text{ag})\ N + NH_2 \rightarrow 2H + N_2 \tag{R6}$$

The increase in the N atom density during the micro-discharges comes from the dissociation of N_2 (Reaction 7), which is in high concentration in the feed. During the afterglow, the N atoms almost solely come from collisions between H and NH (Reaction 8).

$$(\text{md})\quad e^- + N_2 \rightarrow e^- + N + N \tag{R7}$$

$$(\text{ag})\ H + NH \rightarrow H_2 + N \tag{R8}$$

The high electron density in the micro-discharges is a result of ionization of the feed gas ($NH_3 + N_2$) (Reaction 9 and 10), where the NH_3^+ density (not shown on Fig. 6) increases from 10^2 to 10^{12} molecules/cm^3. As the N_2 concentration is roughly 49 times higher than the NH_3 concentration, Reaction 10 contributes to a larger extent to the formation of electrons. However, it only contributes ca. 10 times more, which is attributed to the higher ionization potential of N_2 (15.6 eV ("IST-Lisbon database www.lxcat.net" 2022)) vs NH_3 (10.2 eV ("Hayashi database www.lxcat.net" 2022)).

$$(\text{md})\quad e^- + NH_3 \rightarrow e^- + e^- + NH_3^+ \tag{R9}$$

$$(\text{md})\quad e^- + N_2 \rightarrow e^- + e^- + N_2^+ \tag{R10}$$

Interestingly, the formed NH_3^+ reacts with NH_3 to form NH_4^+ and NH_2 (Reaction 11), thereby contributing to the decomposition. However, the main NH_4^+ destruction reaction is by recombination with an electron (Reaction 12) to form again a stable NH_3 molecule; hence, the formation of NH_3^+ also has a negative effect on the NH_3 decomposition, due to the loss of electron energy in this cycle of electron impact ionization (Reaction 9) and recombination (Reaction 12).

$$(\text{md})\quad NH_3^+ + NH_3 \rightarrow NH_4^+ + NH_2 \tag{R11}$$

$$(\text{md})\quad e^- + NH_4^+ \rightarrow NH_3 + H \tag{R12}$$

Fig. 6c shows the densities of the neutral and vibrationally excited species during two micro-discharges and their afterglows, and Fig. 6d for the radicals and charged species, for the packed reactor. Here, the time in plasma corresponds to the 23rd and 24th micro-discharge encountered by a molecule, as a larger number of micro-discharges occurs per half period compared to the unpacked setup. Furthermore, the lifetime of the afterglows is reduced from 120 ms for the unpacked reactor to 30 ms for the packed bed.

The previously discussed reactions (Reaction 2–12) remain dominant for the packed bed, but some of them become more prominent for the formation or consumption of a given species. Fig. 6c shows that the density of $N_2(v)$ between micro-discharges increases from 1.9×10^{18} (in the unpacked setup, cf. Fig. 6a) to 3.8×10^{18} molecules/cm^3 in the packed setup, but the peak density in the micro-discharges is lower (6.0×10^{18} compared to 7.0×10^{18} molecules/cm^3). This is due to a lower rate of Reaction 2 (by a factor of ca. 2), while the rate of Reaction 3 is increased by a factor of 2.5. Furthermore, only small changes are seen for the N_2 and H_2 densities during a micro-discharge, meaning that the formation rate of N and H is lower for the packed setup compared to the unpacked (Fig. 6). Similar to the unpacked setup, the density of NH_3 is decreasing slowly for the packed setup (barely visible on Fig. 6c). The rate of density change (source term) will be discussed further below.

The plateau concentrations in the afterglows for radicals and charged species seen in Fig. 6 are a result of the non-zero power density distribution. This means that the electrons are continuously heated by a small power deposition, which allows for electron collision reactions, however, at a lower reaction rate compared to during the micro-discharges.

Additionally, the introduction of $MgAl_2O_4$ packing increases the contribution of surface reactions. Indeed, for the unpacked setup, surface reactions can only occur at the reactor wall and inner electrode surface, while in the packed setup, the packing greatly enhances the available surface area. Fig. 7 shows the surface coverage during the 23rd and 24th micro-discharge, similar to Fig. 6c and d. Here, H(s) is determined to be the main adsorbate, which correlates with the adsorption energies at the reaction tempera-

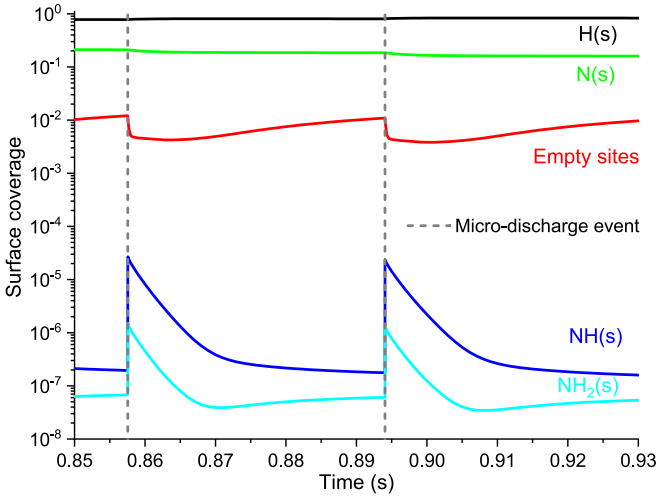

Fig. 7. Calculated surface coverage and fraction of empty sites as a function of time when operating in a packed reactor with an outer electrode length of 5 cm and $\gamma = 0.35$.

ture, and shows a small increase in coverage during the micro-discharges that stays constant during the afterglows. However, during the first few micro-discharges, the H(s) coverage is increasing rapidly due to the formation of H and H_2 from the NH_3 decomposition (see Figure S7). A somewhat similar tendency is observed for N(s) on Fig. 7, with an almost constant coverage during the afterglows. However, in contrast to H(s), the N(s) coverage is slowly decreasing during the micro-discharges and during the first few micro-discharges it is the main adsorbed species on the surface, because of the high N_2 concentration present in the feed gas. A plot of the surface coverage during the complete residence time is shown in the Supporting Information (Figure S7).

In contrast to H(s) and N(s), the NH(s) and NH_2(s) coverage is clearly observed to increase during the micro-discharges with up to two orders of magnitude. For NH_2(s) this is partly due to the fast increase in density of NH_2 in the gas phase that adsorbs on empty surface sites (see Reaction 13) and due to an ER reaction between NH and H(s) (see Reaction 14). For NH(s), the increased coverage is almost solely a result of an ER reaction between N and H(s) (see Reaction 15). During the afterglow, the coverage of both species slowly decreases to a value slightly below the previous afterglow, hence leading to an overall drop in surface coverage of both species over a longer time scale.

$$(\mathrm{md})\quad NH_2 + \mathrm{surf} \rightarrow NH_2(s) \tag{R13}$$

$$(\mathrm{md})\quad NH + H(s) \rightarrow NH_2(s) \tag{R14}$$

$$(\mathrm{md})\quad N + H(s) \rightarrow NH(s) \tag{R15}$$

The decrease in surface coverage of NH(s) during the afterglow is due to its consumption in the formation of NH_2(s), which subsequently forms NH_3 causing a negative effect of the packing material on the NH_3 decomposition. The model thereby predicts that the NH_3 decomposition is taking place in the gas phase and is initiated by electron collisions, mainly during the micro-discharges, but is counteracted by NH_3 formation from NH_2(s) due to the packing during the afterglows. The NH_3 decomposition reaction pathway to H_2 and N_2 will be discussed in further detail in section 4.6.

The current model describes the formation of NH_3 from surface-adsorbed species by desorbing NH_3 as it is formed, and the surface coverage of NH_3 is therefore not determined. Furthermore, the model does not include electronically/vibrationally excited NH_3, and their surface adsorption contribution is therefore also not included.

4.5. Change of species in the micro-discharges and afterglows

The time-averaged net source terms for the various gas phase species, in a single micro-discharge and the following afterglow, are shown in Fig. 8, to identify whether species are produced or removed. The data shown in Fig. 8 is taken from the second to last micro-discharge, since the system has reached a state where the previous cycle (micro-discharge and afterglow) resembles the next cycle. As also observed in Fig. 6, NH_2, NH, H, N, and the electrons are net produced during the micro-discharges for both the unpacked and packed setup (non-patterned compared to patterned bars in Fig. 8) and consumed in the afterglows. For the molecules, NH_3, H_2, and N_2, a net consumption is predicted by the model during the micro-discharges, which for NH_3 also is the case during the afterglows; however, the source term is 6 orders of magnitude smaller in the afterglows (red bar compared to grey bar). Generally, the source term of the species during the afterglows (typically in the order of 10^{16} to 10^{19} cm^{-3} s^{-1}) is found to be smaller than during the micro-discharges (in the order of 10^{21} to 10^{25} cm^{-3} s^{-1}), meaning that the reaction rates are higher in the micro-discharges. Interestingly, H_2 and N_2 are the only two species in Fig. 8 that are produced during the afterglows, indicating that a relaxation period is important for the formation of the desired decomposition products. However, it is during the micro-discharges that the main destruction of NH_3 occurs. Moreover, during the afterglows a net consumption of electrons is found, which is attributed to the lack of ionization collisions. It is therefore likely that there is an optimal discharge frequency for the NH_3 decomposition, which is outside of the range tested in Fig. 3.

Comparing the difference between the unpacked and packed setup in Fig. 8, a generally slightly higher source term during the micro-discharges is predicted for the unpacked setup. This aligns well with the higher density of electrons during micro-discharges for the unpacked setup, as electron-molecule collisions are the dominant reactions in this phase. During the afterglows, the source terms for NH_3, H_2, H, N, and N_2 are almost equal, and for NH_2, NH, and electrons the consumption is slightly higher for the packed setup. The higher consumption of NH comes from adsorption on the surface and from the formation of NH_2(s) via Reaction 14. Similarly for NH_2, adsorption on the surface as well as formation of NH_3 causes the higher consumption.

4.6. NH_3 reaction pathways in micro-discharges and their afterglows

Based on the preceding sections, the reaction pathways for the NH_3 decomposition in a micro-discharge and its afterglow for plasma alone are summarized in Fig. 9. The %-values given within the parentheses in Fig. 9 are normalized with the NH_3 consumption in the specific plasma phenomena, which is also the case for the %-values given in the text of this section. The main reaction for NH_3 is dissociation by collision with an electron, which can yield either NH_2 or NH (Reaction 5 and 16) both in the micro-discharges and afterglows. However, the dissociation to NH_2 occur ca. 3 times faster compared to NH in a micro-discharge, and ca. 5 faster in the afterglow. Additionally, in a micro-discharge a small fraction of NH_3 (2.6 %) is ionized to NH_3^+ (Reaction 9).

$$(\mathrm{md/ag})\quad e^- + NH_3 \rightarrow e^- + NH_2 + H \tag{R5}$$

$$(\mathrm{md/ag})\quad e^- + NH_3 \rightarrow e^- + NH + H_2 \tag{R16}$$

$$(\mathrm{md})\quad e^- + NH_3 \rightarrow e^- + e^- + NH_3^+ \tag{R9}$$

The formed NH_3^+ then almost solely react with NH_3 to form NH_4^+ and NH_2 (Reaction 11). The NH_4^+ then collide with an electron to either re-form NH_3 or form NH_2 (Reaction 12 and 17).

$$(\mathrm{md})\quad NH_3^+ + NH_3 \rightarrow NH_4^+ + NH_2 \tag{R11}$$

$$(\mathrm{md})\quad e^- + NH_4^+ \rightarrow NH_3 + H \tag{R12}$$

$$(\mathrm{md})\quad e^- + NH_4^+ \rightarrow NH_2 + 2H \tag{R17}$$

Subsequently, the formed NH_2 from Reaction 5, 11, and 17 collide with N to form N_2 and two H or H_2 (Reaction 6 and 18), which in a micro-discharge occurs equally (35 %). As explained earlier, the dissociation of N_2 forms N (Reaction 7), hence the N_2 content in the plasma thereby impacts the decomposition of NH_3 due to the use of N in the conversion of NH_2.

In the afterglows two additional reactions (Reaction 19 and 20) contribute significantly to the consumption of NH_2. In Reaction 19, NH_2 reacts with H to form NH_3 and in Reaction 20, NH_2 reacts with H to form H_2 and NH. This yields a contribution of 25 % for Reaction 6 and 18, 18 % for Reaction 19, and 10 % for Reaction 20 in the NH_3 consumption in the afterglows.

$$(\mathrm{md/ag})\quad N + NH_2 \rightarrow 2\,H + N_2 \tag{R6}$$

$$(\mathrm{md/ag})\quad N + NH_2 \rightarrow H_2 + N_2 \tag{R18}$$

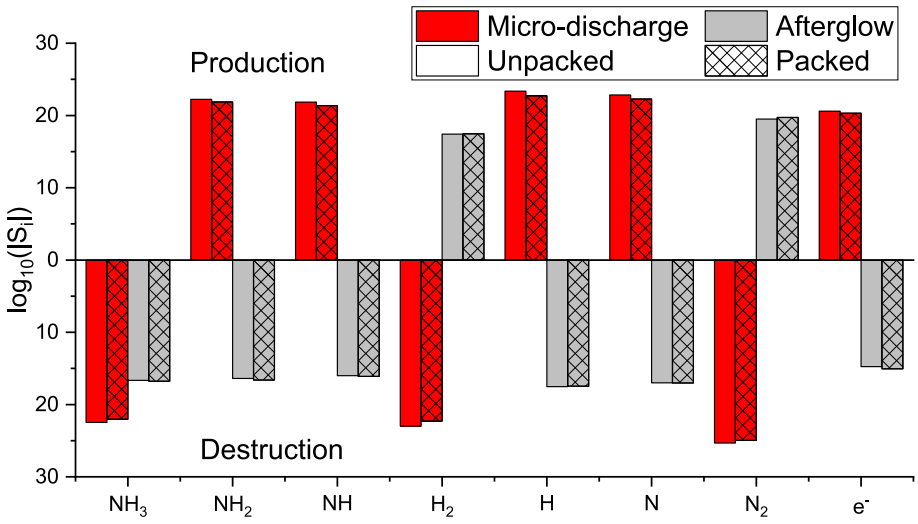

Fig. 8. Time-averaged net source terms (S_i) (cm^{-3} s^{-1}) in the second to last micro-discharge and its subsequent afterglow for the various molecules, radicals, and electrons in the gas phase, for both the packed and unpacked setup (see legend).

$$(\mathrm{ag})\quad \mathrm{H} + \mathrm{N_2} + \mathrm{NH_2} \rightarrow \mathrm{NH_3} + \mathrm{N_2} \tag{R19}$$

$$(\mathrm{ag})\quad \mathrm{H} + \mathrm{NH_2} \rightarrow \mathrm{NH} + \mathrm{H_2} \tag{R20}$$

The remaining 22 % of the NH_3 consumption is through NH reactions. Indeed, the formed NH reacts with H or N to yield H_2 and N (Reaction 8) or H and N_2 (Reaction 21), respectively. Both of these reactions occur in the micro-discharges and afterglows. However, the relative contribution of Reaction 8, compared to 21, is ca. 2 times higher during a micro-discharge, which increases to ca. 9 times in the afterglow. Additionally, Reaction 8 is the main reaction path for H atoms in a micro-discharge, but during the afterglows, the H atoms are mainly consumed in the formation of H_2 by recombination with a second H atom.

$$(\mathrm{md/ag})\quad \mathrm{H} + \mathrm{NH} \rightarrow \mathrm{H_2} + \mathrm{N} \tag{R8}$$

$$(\mathrm{md/ag})\quad \mathrm{N} + \mathrm{NH} \rightarrow \mathrm{H} + \mathrm{N_2} \tag{R21}$$

A small amount of NH also reacts with another NH molecule and yields two H and N_2 (Reaction 22). The relative contribution of Reaction 22 during a micro-discharge (2.4 %) is a result of the high density of NH momentarily present (see Fig. 6). The density then quickly drops in the afterglow, resulting in a lower contribution of Reaction 22 (0.4 %).

$$(\mathrm{md/ag})\quad \mathrm{NH} + \mathrm{NH} \rightarrow 2\,\mathrm{H} + \mathrm{N_2} \tag{R22}$$

The model predicts a similar reaction pathway for NH_3 decomposition when packing material is introduced in the plasma (see Figure S8). As can be seen, the same reactions described for the plasma alone (Reaction 5, 6, 8, 9, 11, 12, and 16 to 22) also dominate for the NH_3 decomposition reaction pathway for the packed setup. However, due to the introduction of a surface, additional reactions occur, such as Reactions 13 to 15. The formed NH(s) from reaction 15 stepwise reacts with H(s), formed from Reaction 23, to produce NH_2(s) (Reaction 24) and finally NH_3 (Reaction 25) both in the micro-discharges and afterglows. However, the combined contribution of these reactions towards the NH_3 conversion are small. During micro-discharges less than 0.1 % and during afterglows ca. 1.6 %. Moreover, in the afterglows, an ER reaction between NH_2 and H(s) contributes to the removal of NH_2, but the product of this reaction is NH_3 (Reaction 26) with a relative negative contribution of 4.9 % in the NH_3 decomposition reaction pathway (see Figure S8). Hence, these surface reactions re-form NH_3, thereby lowering the overall NH_3 decomposition.

$$(\mathrm{md/ag})\quad \mathrm{H} + \mathrm{surf} \rightarrow \mathrm{H(s)} \tag{R23}$$

$$(\mathrm{md/ag})\ \mathrm{NH(s)} + \mathrm{H(s)} \rightarrow \mathrm{NH_2(s)} + \mathrm{surf} \tag{R24}$$

$$(\mathrm{md/ag})\ \mathrm{NH_2(s)} + \mathrm{H(s)} \rightarrow \mathrm{NH_3} + \mathrm{surf} + \mathrm{surf} \tag{R25}$$

$$(\mathrm{ag})\ \mathrm{NH_2} + \mathrm{H(s)} \rightarrow \mathrm{NH_3} + \mathrm{surf} \tag{R26}$$

From the reactions presented in this section, it is evident that the high energy electrons play a crucial role in the conversion of NH_3 by initiating its decomposition. Furthermore, the electrons also form key reactants (N and H) through dissociation in the micro-discharges, which are used in the intermediate steps to decompose NH_x. This importance of high energy electrons correlates well with the experimental observations made from Fig. 2 and Fig. 3 where increased power and frequency lead to an increased conversion. However, in the presence of a surface, the N and H atoms also react with each other or NH_x radicals, through Eley-Rideal and Langmuir-Hinshelwood reactions, to form again NH_3, partially explaining the lower NH_3 decomposition in the packed reactor.

These results are in agreement with the findings of Akiyama et al. (2018) and our previous work on NH_3 decomposition (Andersen et al., 2022), where the decomposition also was concluded to occur mainly in the gas phase by interaction with the high energy electrons. Moreover, in our previous work (Andersen et al., 2022) we observed a linear correlation between the number of micro-discharges and the conversion, which is not the case in this study. This is likely due to the different feed composition used in the two studies, as the collision with N atoms was found to influence the NH_2 conversion greatly in current work (Reaction 6 and 18). These N atoms were not formed in high concentrations with a pure NH_3 feed and could only be formed by converting the feed NH_3. Hence, the rate of the NH_3 decomposition will initially be slower in the absence of N or N_2 because the rate of NH_3 re-formation from NH_2 will be approximately equal to the further dissociation by electron collision in the micro-discharges without N atoms. In the afterglow, with N_2 in the feed, the rate of NH_3 dissociation by electron collision drops below the rate of re-formation of NH_3, and the consumption of the formed H atoms is (in relation to

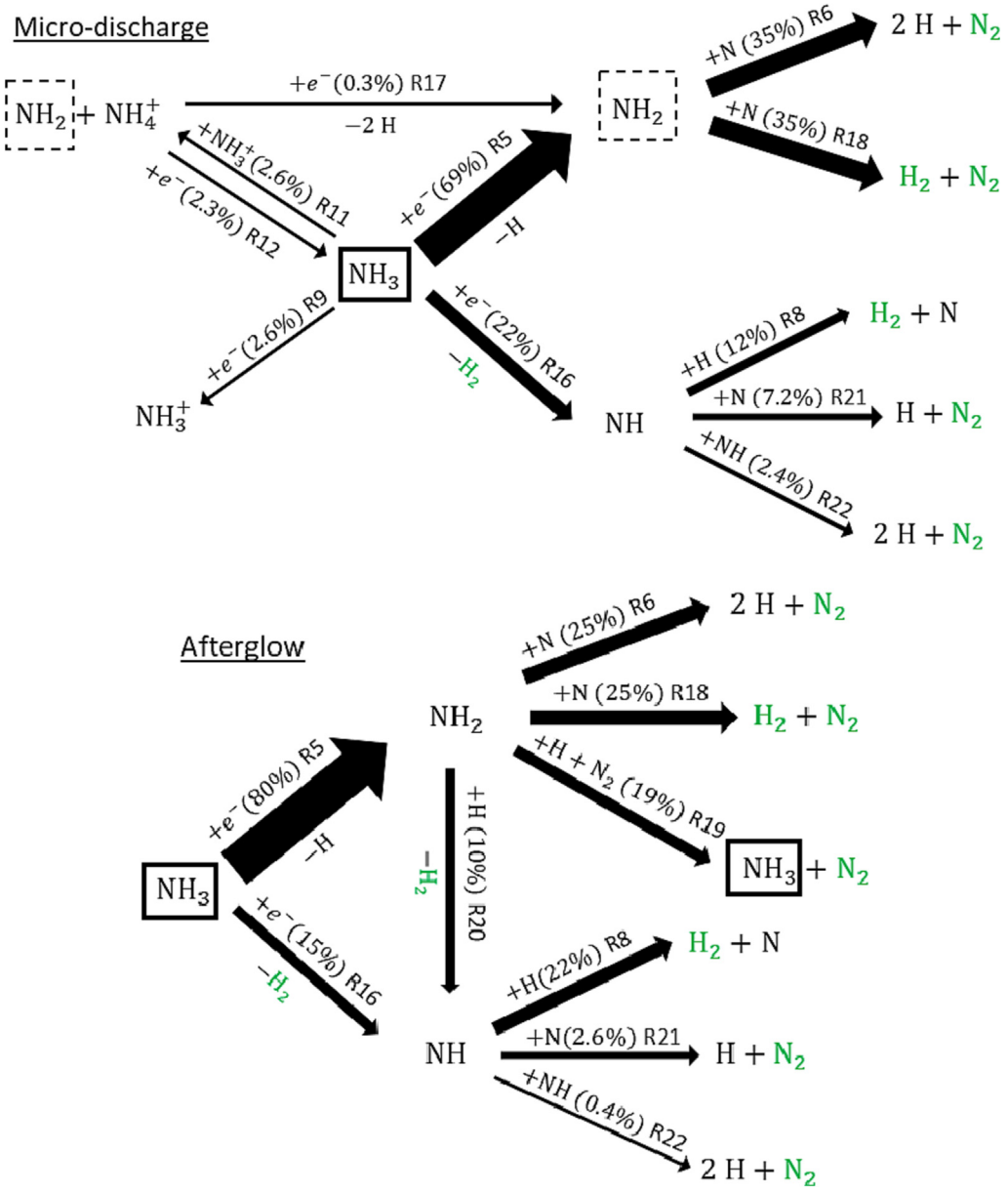

Fig. 9. Schematic reaction pathways for NH_3 decomposition into H_2 and N_2 in a micro-discharge and its afterglow, for plasma-only.

NH_2) predicted to be mainly for re-formation of NH_3 and not dissociative collisions under the experimental conditions. Removing this produced H/H_2 could improve the conversion of NH_3 by limiting the re-formation, as shown by Hayakawa et al. (2020) with a plasma membrane reactor.

As mentioned previously, the model predicts a negative effect of the packing material due to the re-formation of NH_3 from H_2(s), NH (s), and NH_2(s). The adsorption of NH and NH_2 are therefore not expected to increase the N_2 and H_2 formation, as indicated experimentally by Yi et al. (2019), because the surface is mainly covered by H(s) that reacts with the radicals and re-form NH_3. As mentioned earlier, the current model does not include electronically excited NH_3 molecules and how the adsorption of these affects the conversion. Since this was proposed by Wang et al. (2017) and Yi et al. (2019) to be a crucial part of the decomposition, this could be included in future work to yield a more detailed kinetic model, if reliable data are available.

5. Conclusion

A combination of experiments and kinetic modelling were used to study the NH_3 decomposition in an unpacked and packed DBD plasma reactor. The experiments showed that increasing the SEI (higher plasma power or lower flow rate) resulted in a higher NH_3 conversion, and that the same conversion was achieved independent of changes to the flow rate or the plasma power when the SEI was the same. At the highest SEI value (18 kJ/Nl) tested in this study, a conversion of 82 % was achieved. Additionally, the NH_3 conversion was found to increase from 44 to 57 % upon rising the frequency from 1.0 to 3.5 kHz.

Furthermore, a change in the plasma distribution, i.e. the fraction of plasma power transferred through micro-discharges or as a uniform plasma, was observed when the electrode length (discharge volume) was altered at a constant plasma power. Here, smaller volume were found to result in a more non-uniform

plasma with a larger number of micro-discharges per volume. This makes it difficult to investigate the pure effect of the gas residence time in the plasma, as the plasma behavior also changes if the residence time is altered through flow rate or electrode length changes. However, it was discovered that a more non-uniform plasma, characterized by more intense micro-discharges, promotes the NH_3 decomposition, which indicates that it is collisions with the high-energy electrons that initiate the decomposition of NH_3. This observation was confirmed by analyzing the contributions of the different reactions in the NH_3 decomposition reaction network predicted by the kinetic model. Here, it was identified that the main conversion of NH_3 occurs due to collision with electrons in the micro-discharges and their afterglows. Overall, a good agreement between the experimental and model-predicted NH_3 conversion could be obtained, when using an appropriate value of the power distribution factor (γ). For the studied conditions, γ was found to change from 0.2 to 0.1 as the plasma volume was changed from 31 to 10 cm^3.

The introduction of packing material resulted in a lower conversion (X_{NH_3} = 37 % at 2.0 s) when compared at a comparable residence time and identical power as for the plasma alone (X_{NH_3} = 51 % at 2.5 s). Yet, the seemingly small reduction in residence time with packing material was observed to be part of the reason for the lower NH_3 conversion. Furthermore, a more uniform plasma was formed by the packing material, with a lower electron density during micro-discharges and a lower average electron energy during the afterglows, which also was found to reduce the NH_3 conversion.

Moreover, the net rate of NH_3 destruction was found to be 5 to 6 orders of magnitude higher during a micro-discharge than during the afterglow for both the unpacked and packed setup. Indeed, a considerable re-formation of NH_3 was found to take place during the afterglow, leading to a stable conversion of NH_3 after a residence time of 13 s (47 % at the conditions of 15 W plasma power, 3 kHz frequency, and 100 Nml/min feed flow rate). The model further identified that N and H radicals are key reactants in the intermediate steps of the decomposition for converting NH_2 and NH. Furthermore, the packing material was found to introduce high concentrations of H(s), which led to significant re-formation of NH_3 through an Eley-Rideal reaction with NH_2 causing a negative effect of the packing on NH_3 conversion.

CRediT authorship contribution statement

J.A. Andersen: Conceptualization, Methodology, Software, Validation, Formal analysis, Investigation, Data curation, Writing – original draft, Visualization. **K. van 't Veer:** Software, Validation, Writing – review & editing. **J.M. Christensen:** Conceptualization, Writing – review & editing, Supervision. **M. Østberg:** Resources, Writing – review & editing, Supervision. **A. Bogaerts:** Resources, Writing – review & editing, Visualization, Supervision. **A.D. Jensen:** Conceptualization, Resources, Writing – review & editing, Visualization, Supervision.

Data availability

Data will be made available on request.

Declaration of Competing Interest

The authors declare that they have no known competing financial interests or personal relationships that could have appeared to influence the work reported in this paper.

Acknowledgments

We thank Topsoe A/S for providing the packing material used, the research group PLASMANT (UAntwerpen) for sharing their plasma kinetic model and allowing us to perform the calculations on their clusters, and the Department of Chemical and Biochemical Engineering, Technical University of Denmark, for funding this project.

Appendix A. Supplementary material

Supplementary data to this article can be found online at https://doi.org/10.1016/j.ces.2023.118550.

References

Akiyama, M., Aihara, K., Sawaguchi, T., Matsukata, M., Iwamoto, M., 2018. Ammonia decomposition to clean hydrogen using non-thermal atmospheric-pressure plasma. Int. J. Hydrogen Energy 43, 14493–14497. https://doi.org/10.1016/j.ijhydene.2018.06.022.

Andersen, J.A., Christensen, J.M., Østberg, M., Bogaerts, A., Jensen, A.D., 2022. Plasma-catalytic ammonia decomposition using a packed-bed dielectric barrier discharge reactor. Int. J. Hydrogen Energy. 47 (75), 32081–32091.

Bai, M., Zhang, Z., Bai, X., Bai, M., Ning, W., 2003. Plasma Synthesis of Ammonia With a Microgap Dielectric Barrier Discharge at Ambient Pressure. IEEE Trans. PLASMA Sci. 31, 1285–1291. https://doi.org/10.1109/TPS.2003.818761.

Bogaerts, A., 2019. Editorial Catalysts: Special Issue on Plasma Catalysis. Catalysts 9 (2), 196.

Bogaerts, A., Neyts, E.C., 2018. Plasma Technology: An Emerging Technology for Energy Storage. Acs Energy Lett. 3, 1013–1027. https://doi.org/10.1021/acsenergylett.8b00184.

Bogaerts, A., Wang, W., Berthelot, A., Guerra, V., 2016. Modeling plasma-based CO_2 conversion: crucial role of the dissociation cross section. Plasma Sources Sci. Technol. 25,. https://doi.org/10.1088/0963-0252/25/5/055016 055016.

Bogaerts, A., Tu, X., Whitehead, J.C., Centi, G., Lefferts, L., Guaitella, O., Azzolina-Jury, F., Kim, H.-H., Murphy, A.B., Schneider, W.F., Nozaki, T., Hicks, J.C., Rousseau, A., Thevenet, F., Khacef, A., Carreon, M., 2020. The 2020 plasma catalysis roadmap. J. Phys. D. Appl. Phys. 53 (44), 443001.

Conrads, H., Schmidt, M., 2000. Plasma generation and plasma sources. Plasma Sources Sci. Technol 9 (4), 441–454.

Cortright, R.D., Dumesic, J.A., 2001. Kinetics of Heterogeneous Catalytic Reactions: Analysis of Reaction Schemes. Adv. Catal. 46, 161–264.

Edwards, P.P., Kuznetsov, V.L., David, W.I.F., 2007. Hydrogen energy. Philos. Trans. R. Soc. A 365, 1043–1056. https://doi.org/10.1098/rsta.2006.1965.

El-Shafie, M., Kambara, S., Hayakawa, Y., 2020. Alumina particle size effect on H_2 production from ammonia decomposition by DBD plasma. Energy Reports 6, 25–30. https://doi.org/10.1016/j.egyr.2020.10.032.

El-Shafie, M., Kambara, S., Hayakawa, Y., 2021. Plasma-enhanced catalytic ammonia decomposition over ruthenium (Ru/Al_2O_3) and soda glass (SiO_2) materials. J. Energy Inst. 99, 145–153. https://doi.org/10.1016/j.joei.2021.09.001.

Engelmann, Y., van 't Veer, K., Gorbanev, Y., Neyts, E.C., Schneider, W.F., Bogaerts, A., 2021. Plasma Catalysis for Ammonia Synthesis: A Microkinetic Modeling Study on the Contributions of Eley−Rideal Reactions. Acs Sustain. Chem. Eng. 9 (39), 13151–13163.

Hagelaar, G.J.M., Pitchford, L.C., 2005. Solving the Boltzmann equation to obtain electron transport coefficients and rate coefficients for fluid models. Plasma Sources Sci. Technol. 14, 722–733. https://doi.org/10.1088/0963-0252/14/4/011.

Hasan, M.H., Meurah, T., Mahlia, I., Mofijur, M., Fattah, I.M.R., Handayani, F., Ong, H. C., Silitonga, A.S., 2021. A Comprehensive Review on the Recent Development of Ammonia as a Renewable Energy Carrier. Energies 14, 3732. https://doi.org/10.3390/en14133732.

Hayakawa, Y., Kambara, S., Miura, T., 2020. Hydrogen production from ammonia by the plasma membrane reactor | Elsevier Enhanced Reader. Int. J. Hydrogen Energy 45, 32082–32088. https://doi.org/10.1016/j.ijhydene.2020.08.178.

Hayashi database www.lxcat.net retrieved in June [WWW Document], 2022.

Hong, J., Prawer, S., Murphy, A.B., 2018. Plasma Catalysis as an Alternative Route for Ammonia Production: Status, Mechanisms, and Prospects for Progress. Acs Sustain. Chem. Eng. 6, 15–31. https://doi.org/10.1021/acssuschemeng.7b02381.

Iriawan, H., Andersen, S., Zhang, X., Comer, B.M., Barrio, J., Chen, P., Medford, A., Chorkendorff, I., Shao-Horn, Y., 2021. Methods for Nitrogen Activation by Reduction and Oxidation. Nat. Rev. Methods Prim. 1, 56. https://doi.org/10.1038/s43586-021-00053-y.

IST-Lisbon database www.lxcat.net retrieved in June [WWW Document], 2022.

Klerke, A., Klitgaard, S.K., Fehrmann, R., 2009. Catalytic Ammonia Decomposition Over Ruthenium Nanoparticles Supported on Nano-Titanates. Catal. Letters 130, 541–546. https://doi.org/10.1007/s10562-009-9964-4.

Lamb, K.E., Dolan, M.D., Kennedy, D.F., 2019. Ammonia for hydrogen storage; A review of catalytic ammonia decomposition and hydrogen separation and

purification. Int. J. Hydrogen Energy 44, 3580–3593. https://doi.org/10.1016/j.ijhydene.2018.12.024.
Lendzion-Bielun, Z., Narkiewicz, U., Arabczyk, W., 2013. Cobalt-based catalysts for ammonia decomposition. Materials (Basel). 6, 2400–2409. https://doi.org/10.3390/ma6062400.
Lucentini, I., García Colli, G., Luzi, C.D., Serrano, I., Martínez, O.M., Llorca, J., 2021. Catalytic ammonia decomposition over Ni-Ru supported on CeO2 for hydrogen production: Effect of metal loading and kinetic analysis. Appl. Catal. B Environ. 286,. https://doi.org/10.1016/J.APCATB.2021.119896 119896.
Pancheshnyi, S., Eismann, B., Hagelaar, G.J.M., Pitchford, L.C., 2008. Computer code ZDPlasKin [WWW Document]. URL http://www.zdplaskin.laplace.univ-tlse.fr/.
Salmon, N., Bañares-Alcántara, R., 2021. Green ammonia as a spatial energy vector: a review. Sustain. Energy Fuels 5, 2814–2839. https://doi.org/10.1039/d1se00345c.
Schüth, F., Palkovits, R., Schlögl, R., Su, D.S., 2012. Ammonia as a possible element in an energy infrastructure: catalysts for ammonia decomposition. Energy & Environmental Sci. 5, 6278–6289. https://doi.org/10.1039/c2ee02865d.
Shannon, R.D., Rossman, G.R., 1991. Dielectric constant of $MgAl_2O_4$ spinel and the oxide additivity rule. J. Phys. Chem. Solids 52 (9), 1055–1059.
Silva, H., Nielsen, M.G., Fiordaliso, E.M., Damsgaard, C.D., Gundlach, C., Kasama, T., Chorkendorff, I., Chakraborty, D., 2015. Synthesis and characterization of Fe–Ni/ɣ-Al_2O_3 egg-shell catalyst for H_2 generation by ammonia decomposition. Appl. Catal. A Gen. 505, 548–556.
Simonsen, S.B., Chakraborty, D., Chorkendorff, I., Dahl, S., 2012. Alloyed Ni-Fe nanoparticles as catalysts for NH_3 decomposition. Appl. Catal. A Gen. 447–448, 22–31. https://doi.org/10.1016/j.apcata.2012.08.045.
Snoeckx, R., Bogaerts, A., 2017. Plasma technology - a novel solution for CO_2 conversion? Chem. Soc. Rev. 46, 5805–5863. https://doi.org/10.1039/c6cs00066e.
van 't Veer, K., Engelmann, Y., Reniers, F., Bogaerts, A., 2020a. Plasma-Catalytic Ammonia Synthesis in a DBD Plasma: Role of Microdischarges and Their Afterglows. J. Phys. Chem. C 124 (42), 22871–22883.
van 't Veer, K., Reniers, F., Bogaerts, A., 2020b. Zero-dimensional modelling of unpacked and packed bed dielectric barrier discharges: The role of vibrational kinetics in ammonia synthesis. Plasma Sources Sci. Technol. 29, 45020. https://doi.org/10.1088/1361-6595/ab7a8a.
Wan, Z., Tao, Y., Shao, J., Zhang, Y., You, H., 2021. Ammonia as an effective hydrogen carrier and a clean fuel for solid oxide fuel cells. Energy Convers. Manag. 228,. https://doi.org/10.1016/j.enconman.2020.113729 113729.
Wang, L., Yi, Y., Zhao, Y., Zhang, R., Zhang, J., Guo, H., 2015. NH_3 Decomposition for H_2 Generation: Effects of Cheap Metals and Supports on Plasma-Catalyst Synergy. ACS Catal. 5, 4167–4174. https://doi.org/10.1021/acscatal.5b00728.
Wang, L., Yi, Y., Guo, Y., Zhao, Y., Zhang, J., Guo, H., 2017. Synergy of DBD plasma and Fe-based catalyst in NH_3 decomposition: Plasma enhancing adsorption step. Plasma Process. Polym. 14, 1600111. https://doi.org/10.1002/ppap.201600111.
Wang, L., Yi, Y., Guo, H.C., Du, X.M., Zhu, B., Zhu, Y.M., 2019. Highly dispersed co nanoparticles prepared by an improved method for plasma-driven NH_3 decomposition to produce H_2. Catalysts 9, 1–13. https://doi.org/10.3390/catal9020107.
Whitehead, J.C., 2016. Plasma–catalysis: the known knowns, the known unknowns and the unknown unknowns. J. Phys. D. Appl. Phys. 49 (24), 243001.
Yi, Y., Wang, L., Guo, Y., Sun, S., Guo, H., 2019. Plasma-assisted ammonia decomposition over Fe–Ni alloy catalysts for COx-Free hydrogen. AIChE J. 65, 691–701. https://doi.org/10.1002/aic.16479.
Zhang, Q.-Z., Bogaerts, A., 2018. Propagation of a plasma streamer in catalyst pores. Plasma Sources Sci. Technol. 27,. https://doi.org/10.1088/1361-6595/aab47a 035009.
Zheng, W., Zhang, J., Ge, Q., Xu, H., Li, W., 2008. Effects of CeO_2 addition on Ni/Al_2O_3 catalysts for the reaction of ammonia decomposition to hydrogen. Appl. Catal. B Environ. 80, 98–105. https://doi.org/10.1016/j.apcatb.2007.11.008.